WSS/CI 95F-223

Numerical Study of Flickering Frequency and Emission Index of a Methane Diffusion Flame for Varying Gravitational Force

C. G. Yam and K. D. Marx
Combustion Research Facility
Sandia National Laboratories

J.-Y. Chen and C.-P. Chou
Mechanical Engineering Department
University of California, Berkeley

Presented at the 1995 Fall Meeting of the
Western States Section/The Combustion Institute
Stanford University, Palo Alto, California, October 30-31, 1995

Sandia National Laboratories

Numerical Study of Flickering Frequency and Emission Index of a Methane Diffusion Flame for Varying Gravitational Force

Clement G.Yam[1], Kenneth D. Marx[1], Jyh-Yuan Chen[2] and Chen-Pang Chou[2]

Abstract

The effects of various magnitudes of gravitational force on the natural flickering frequency and the emission indexes of NO_x and CO of an unsteady laminar methane diffusion flame are investigated numerically. This is done by solving the low Mach number formulation of the time-dependent Navier-Stokes equations. A staggered mesh in cylindrical coordinates with a numerical algorithm that is accurate to second order in both time and space is used. Free outflow boundary conditions that allow mass to enter or exit the computational domain are employed in this study. This allows the placement of the outer boundary of the computational domain close to the region of interest. For a given number of grid points, it is then more computationally efficient to utilize a relatively fine grid, which reduces numerical dissipation to a minimum. In order to solve this elliptic time-dependent reacting flow problem rapidly, the complex chemical mechanism is simplified by using the concept of a flamelet model originally developed for non-premixed turbulent combustion. By using a flamelet library, the solution of only one additional transport equation, that for the mixture fraction, is required. This enables us to avoid solving the energy and species equations, which would necessitate the resolution of chemical time and spatial scales that are much smaller than the characteristic fluid time scale. The first five seconds of the formation of a diffusion flame under various gravitational constants is simulated in this study. The calculation is started with the injection of both fuel and air into an initially quiescent domain. A diffusion flame is assumed to be formed immediately at the stoichiometric region. Due to the heat release from the combustion, the density near the reaction zone is a factor of seven lower than the surrounding air. This leads to the domination of the entire flow field by the buoyancy force. As the flow develops, the flame grows rapidly to an expected height, but never reaches a steady state. This is due to the introduction of an instability in the flow field by the shearing action between the hot burned gases and the cold coflowing air. This instability takes the form of a flame flickering with a natural frequency. The calculated flickering frequency under the normal gravitational force of 1 g was then compared with experimental data with reasonable agreement. Gravitational forces of 0.5 g and 2.0 g are also investigated in this work. As anticipated, it is observed that both the flame height and the flickering frequency are functions of the gravitational constant [1]. Following the approach used by other researchers, linear stability analysis is applied to gain insight into the physical nature of the flickering behavior. Instantaneous and time-averaged emission indexes (EI) of NO_x and CO are de-

[1] Combustion Research Facility, Sandia National Laboratories, Livermore, California
[2] University of California, Berkeley

termined at the exit plane of the computational domain. It is found that as the gravitational forces increase, the mean NO_x emission index decreases, while that for CO increases. Moreover, the instantaneous emission index of NO_x and CO are in phase under the range of gravitational forces that we have studied.

1. Introduction

Numerical simulation of low Mach number unsteady flows is a difficult task due to the elliptic nature of the governing equations. When coupled with chemical reactions, the flow is further characterized by multiple time and spatial scales associated with chemical kinetics. Not only does one need to resolve the fluid time scale, but it is also necessary to resolve the chemical time scale. For fuels involving fast chemistry (hydrogen is an excellent example for subsonic flows), it is often satisfactory to assume that chemical kinetics is in equilibrium to avoid the solution of the energy and species equations[2]. For most hydrocarbon fuels, however, the equilibrium assumption produces a flame temperature 10 percent greater than that obtained from a finite-rate kinetics calculation. As the molecular weight of the hydrocarbon fuel increases, results from equilibrium and finite-rate kinetics calculations deviate further. This is because as the molecules become more complex, more intermediate reaction steps are needed to reach the final products, each one of which requires finite time. When unsteady reacting flow with hydrocarbon fuel and finite-rate kinetics is required, even the most powerful supercomputers will limit the type of flow and chemistry one can realistically simulate. Alternate methods such as one-step fast chemistry and reduced mechanisms have been developed to cut down the CPU time and memory. Stiffness still restricts the size of the time step and limits the saving of CPU time. Here, an approach drawing from the concept of a flamelet model originally developed for non-premixed turbulent combustion by Peters [3] is introduced. This approach, the flamelet library concept, promises dramatic saving in both CPU time and memory.

The flamelet library concept allows the decoupling of the flow field calculation from the detailed chemistry calculation. A chemistry library called the 'flamelet library' can be constructed prior to the flow field calculation. This flamelet library provides thermochemical properties involved in the flow field calculations, such as density ρ, viscosity μ, diffusivity D, temperature T, and species concentrations. The coupling between chemistry and fluid flow is modeled through two variables, mixture fraction f and the scalar dissipation rate χ. To build such a library, one needs to perform detailed chemistry calculations for the species and energy equations with f and χ as the independent variables. Then all of the numerical results are compiled into one library file. During the flow field computation, the continuity equation and the momentum equations are solved simultaneously along with the mixture fraction equation which does not contain any source term. The density is evaluated as a function of f and χ from the flamelet library.

Most previous numerical studies [4, 5] of unsteady flames are initialized with a uniform flow condition within the domain of interest. Variations in temperature and density are

then slowly introduced into the simulation. Although this is satisfactory to determine the flickering frequency of the flame, this type of calculation avoids the development of the flame, which is difficult to simulate. This is because the velocity field has an initial value of zero magnitude everywhere, and the system is subject to a rapid change in density (e.g., by a factor of seven) resulting from the flame front propagating downstream. The numerical scheme must be accurate and stable enough to resolve the rapid changes of the flow field. The present study simulates the first five seconds of the formation of a methane jet diffusion flame exhibiting rapid expansion of a hot reacting jet injected into a cold still air environment. The ability to simulate the early formation of this expanding reacting jet indicates that the method employed is stable and robust enough to study various kinds of unsteady reacting flows.

The origin of the oscillation of this and similar flames is the Kelvin-Helmholtz instability which occurs because of the shear between the rapidly rising hot gases and the cold surrounding air. After a discussion of the results of the numerical simulation of the flame, we present an approximate analysis of this instability, and show that it permits a crude estimate of the flickering frequency.

2. Problem of Interest

In this study, the co-annular axisymmetric burner used in the experiments of Smyth, et al. [6] is modeled. It has a fuel diameter of 1.1 cm surrounded by an annulus of coflowing air with an outer diameter of 10.2 cm. The mean methane cold flow and the air coflow velocities are both 7.9 cm/s. The computational domain covers a region of outer radius of 20 cm and an axial distance of 45 cm. A total of 52 by 122 grid points in the radial and axial directions, respectively, are used. Numerical results of flame height in the quasi-steady state, the natural flickering frequency, and emission indexes for NO_X and CO under various magnitudes of gravitational force will be discussed.

3. Governing Equations

For very slow speed (subsonic) flows ($U_\infty << a$, where U_∞ is the characteristic velocity and a is the local sound speed), it can be shown that the momentum equation will approach a singular point when the Mach number (M) approaches zero. One method of solving this problem is to decompose all variables into a power series of ε, where $\varepsilon \sim M^2$, and is assumed to be smaller than one. The decomposed variables are then substituted back into the governing equations. Terms of similar magnitude are then collected. One can see that the pressure field can be split into thermodynamic pressure (which is constant in space and is defined by the equation of state) and the dynamic pressure (which appears in the momentum equation):

$$P_{Total} = P_{Thermal} + P_{Dynamic}$$

with

$$P_{Thermal} = \rho RT.$$

The time-dependent governing equations with the low Mach number assumption are:

I. Continuity Equation:

$$\frac{\partial \rho}{\partial t} + \vec{\nabla} \bullet \left(\rho \vec{V}\right) = 0$$

where ρ is density, t is time, and $\vec{V}$ is the velocity vector.

II. Momentum Equation:

$$\rho \frac{\partial \vec{V}}{\partial t} + \rho \vec{V} \bullet \vec{\nabla} \vec{V} = -\vec{\nabla} P + \vec{\nabla} \bullet \vec{\tau} + \rho \vec{g}$$

where P is the dynamic pressure, $\vec{g}$ is the gravitational vector, and $\vec{\tau}$ is the stress tensor:

$$\tau_{ij} = \mu \left(\frac{\partial u_i}{\partial x_j} + \frac{\partial u_j}{\partial x_i} - \frac{2}{3} \delta_{ij} \vec{\nabla} \bullet \vec{V} \right)$$

III. Mixture fraction equation:

$$\rho \frac{\partial f}{\partial t} + \rho \vec{V} \bullet \vec{\nabla} f = \vec{\nabla} \bullet \left(\rho D \vec{\nabla} f\right)$$

where f is the mixture fraction and D is the diffusion coefficient.

4. Flamelet model

The concept of the flamelet library is an extension of the laminar flamelet concept proposed by Zel'dovich and Frank-Kamenetskii [7] in 1938. This idea is based on the assumption that if the chemical time scale is short compared to the convection and diffusion time scales, combustion takes place within asymptotically thin layers called flamelets. Because the chemical time scale is much smaller than the characteristic fluid time scale in the flow field, the chemistry is in a quasi-steady state and can be considered separately from the flow field. A detailed description of the laminar flamelet concept can be found in the review paper by Peters [3]. The flamelet library concept preserves the essential idea of the flamelet model, i.e., the independence of the flow field and the chemistry. But instead of treating the flamelet as a flame sheet and assuming local chemical equilibrium, the flamelet library concept involves the calculation of the inner structure of the flamelet by stretching out the coordinate perpendicular to the flame front and saving all the informa-

tion in a library. Following the procedure described in [3], one can transform the energy and the species equations from the original spatial coordinate system (t,x_1,x_2) to a coordinate system attached to the surface of stoichiometric mixture (t, f, x_2). The mixture fraction f is a conserved scalar and is a function of space (x_1,x_2) and time t. According to the flamelet theory, derivatives with respect to x_2 are of lower order compared to the derivatives with respect to f in the thin inner reaction zone, i.e.

$$\frac{\partial}{\partial f} >> \frac{\partial}{\partial x_2} \tag{1}$$

Hence, the transformation rules become

$$\frac{\partial}{\partial t} = \frac{\partial}{\partial t} + \frac{\partial f}{\partial t}\frac{\partial}{\partial f} \tag{2}$$

and

$$\frac{\partial}{\partial x_i} \approx \frac{\partial f}{\partial x_i}\frac{\partial}{\partial f} \qquad i = 1,2. \tag{3}$$

Substituting the above expressions into the species equation and the energy equation yields

Species Equation :

$$\rho\frac{\partial Y_k}{\partial t} = \rho\frac{\chi}{2}\frac{\partial^2 Y_k}{\partial f^2} + \dot{\omega}_k W_k \tag{4}$$

Energy Equation :

$$\rho\frac{\partial T}{\partial t} = \rho Le\frac{\chi}{2}\frac{\partial^2 T}{\partial f^2} - \sum_k \frac{\rho\dot{\omega}_k h_k}{Cp} \tag{5}$$

where

$$\chi = 2D\frac{\partial f}{\partial x_i}\frac{\partial f}{\partial x_i} \qquad i = 1,2 \tag{6}$$

is the scalar dissipation rate and

$$Le = \frac{\lambda}{\rho DCp} \tag{7}$$

is the Lewis number. The scalar dissipation rate χ has the units sec^{-1} and may be interpreted as the inverse of a characteristic diffusion time.

The flamelet formulation leads to a one-dimensional structure normal to the surface of stoichiometric mixture. The unsteady terms in equations (4) and (5) can be neglected by assuming the quasi-steady burning state in the reaction zone. Note that the assumption of a quasisteady state in the flamelet will become inappropriate when the flame is close to quenching or the characteristic time scale in the flow field is very short.

By assigning different values of χ, equations (4) and (5) are solved with detailed chemistry and the results are used to construct the library file. These equations are stiff; they are solved by Newton iteration with local grid refinement. The resulting flamelet library is then used in the reacting flow code described in the following section.

5. Numerical Method

I) Numerical scheme

Cylindrical coordinates with a staggered mesh are used in this study. Radial velocity u and axial velocity w are defined at the left and right, upper and lower cell surfaces, respectively, while density ρ, pressure P, and mixture fraction f are defined at the cell centers. To minimize numerical diffusion, a second order upwind scheme [8] is used for the convective terms. A second-order central differencing is used for the diffusion term. A second-order backward differencing (Adams-Bashforth) is also used to advance the solution in time. A semi-explicit scheme similar to Kim and Moin [9] is used to solve for the variables at the new time level, but with an iterative scheme to solve for the pressure field.

II) Pressure solver

The governing equations consist of the continuity equation, two momentum equations for the velocities u and w, and a transport equation for the mixture fraction f. The density field is obtained from the flamelet library. However, we do not have an explicit equation for the pressure P. The method that was used to obtain pressure in this study is a variation of the projection method developed by Chorin [10]. The present method involves solving the momentum equations using predictor-corrector steps as follows.:

Step 1: Predictor

By using the velocity field at time levels n and n-1, and density and pressure at level n, a provisional velocity field $\hat{\vec{V}}$ is then obtained by:

$$\frac{\hat{\rho}\hat{\vec{V}} - \rho^n \vec{V}^n}{\Delta t} = -\vec{\nabla} p^n - \left(\rho \vec{V} \bullet \vec{\nabla} \vec{V}\right)^{n, n-1} + \left(\vec{\nabla} \bullet \vec{\tau}\right)^{n, n-1} + 0.5 \times (\hat{\rho} + \rho^n)\vec{g}$$

Step 2: Corrector

Assuming that the pressure correction α is known such that $p^{n+1} = p^n + \alpha$, a corrected velocity $\vec{V}^{n+1}$ can be determined by:

$$\frac{\rho^{n+1}\vec{V}^{n+1} - \hat{\rho}\hat{\vec{V}}}{\Delta t} = -\vec{\nabla}\alpha .$$

The next step is to evaluate the pressure correction α by using the continuity equation.

$$\frac{\partial \rho}{\partial t} + \vec{\nabla} \bullet (\rho^{n+1}\vec{V}^{n+1}) = 0 .$$

Letting $\vec{V}^{n+1} = \hat{\vec{V}} + \vec{V}_c$, where $\hat{\vec{V}}$ is the provisional velocity field obtained from step 1, the continuity equation can be rewritten as:

$$\frac{\partial \rho}{\partial t} + \vec{\nabla} \bullet (\rho^{n+1}\hat{\vec{V}}) + \vec{\nabla} \bullet (\rho^{n+1}\vec{V}_c) = 0 .$$

By defining a scalar ϕ such that $-\vec{\nabla}\phi = \rho^{n+1}\vec{V}_c$, and substituting for $\vec{V}_c$, a Poisson equation for ϕ is obtained:

$$\frac{\partial \rho}{\partial t} + \vec{\nabla} \bullet (\rho^{n+1}\hat{\vec{V}}) = \nabla^2 \phi .$$

The final step in this method is to relate the scalar ϕ to the pressure correction α by using the step 2 of solving the momentum equation. By substituting the definition of $\vec{V}^{n+1} = \hat{\vec{V}} + \vec{V}_c$, we have

$$\frac{\rho^{n+1}\vec{V}^{n+1} - (\hat{\rho}\vec{V}^{n+1} - \hat{\rho}\vec{V}_c)}{\Delta t} = -\vec{\nabla}\alpha .$$

Then

$$\frac{\hat{\rho}\vec{V}_c}{\Delta t} = -\vec{\nabla}\alpha$$

and

$$\frac{\vec{\nabla}\phi}{\Delta t} = \vec{\nabla}\alpha$$

or $\dfrac{\phi}{\Delta t} = \alpha$ and $\vec{V}_c = -\dfrac{1}{\rho^{n+1}}\vec{\nabla}\phi$.

Since all transport properties and density are functions of mixture fraction and the scalar dissipation rate alone, and both ρ and f are unknown at the new time level for the mixture fraction equation, special care is needed to deal with the nonlinear mixture fraction equation, which can be written as:

$$\frac{\rho^{n+1} f^{n+1} - \rho^{n} f^{n}}{\Delta t} = \left(RHS\right)^{n, n-1},$$

where $RHS = -\vec{\nabla} \bullet (\rho \vec{V} f) + \vec{\nabla}(\rho D \vec{\nabla} f)$. Then the mixture fraction at the *n+1* level can be obtained by the following linear equation:

$$f^{n+1} = \frac{\rho^{n} f^{n} + \Delta t \times \left(RHS\right)^{n, n-1}}{\rho^{n+1}},$$

where the new density is obtained by performing a first-order Euler expansion in time:

$$\rho^{n+1} = \rho^{n} + \left.\frac{\partial \rho}{\partial t}\right|^{n} \Delta t.$$

III) Initial and Boundary Conditions

At time equal to zero, the velocity is initialized to zero everywhere. The density is set to that of cold air. As time elapses, velocity and density are varied according to prescribed values at the inlet boundary. The mixture fraction is set equal to unity at the fuel inlet. At the outer radial boundary and at the downstream boundary, a free-flow boundary condition is imposed (i.e., the second derivatives of all variables are set equal to zero). Due to the large change in density between the hot combustion products and the cold air, the inlet velocity and mixture fraction are "slowly" increased from zero to its maximum in 50 ms to 120 ms. The inlet condition is then held constant for the rest of the simulation. Symmetry boundary conditions are imposed at the axis.

Since ϕ is related to the velocity correction and since the velocity at all the boundaries (except at the outflow boundaries) are known, the velocity corrections are equal to zero.

This implies that the normal gradient of ϕ is zero. At the outflow boundaries, since we do not know the velocity, special treatment is required. This is done by first applying the Poisson equation to the entire domain

$$\iiint\left(\nabla^2\phi\right)dV = \iiint\left[\frac{\partial\rho}{\partial t} + \vec{\nabla}\bullet(\rho^{n+1}\hat{V})\right]dV .$$

Applying Gauss' theorem, the above equation becomes

$$\iint\vec{\nabla}\phi\bullet\vec{n}dA = \iiint\left[\frac{\partial\rho}{\partial t} + \vec{\nabla}\bullet(\rho^{n+1}\hat{V})\right]dV .$$

Since $\vec{\nabla}\phi\bullet\vec{n}dA$ is zero at the inlet and on the axis, the gradient of ϕ at the outflow boundaries can then be determined by the right hand side of the above equation.

IV) Stability

Due to the explicit nature of the numerical scheme, it is necessary to satisfy a stability criterion. Since we are using the flamelet library to obtain changes in density and temperature, the chemistry time scale need not be resolved. Thus the only time scale of concern is that of convection. The time step Δt^n is then calculated by:

$$\Delta t^n = \sigma\min_{ij}\left(\frac{\Delta r_j}{u^n_{i,k}}, \frac{\Delta z_k}{w^n_{i,k}}\right)$$

where σ is the CFL number and is less than unity.

6. Discussion of results

I) Accuracy

A series of test problems was performed to verify the code. First, an isothermal flow in a pipe with pure potential flow as the inlet condition was computed. The computed fully developed, steady-state solution was then compared with the analytical solution. The difference between the numerical results and the analytical results were within discretization error. Second, a confined steady-state reacting flow simulated by Keyes, et al. [11] was recomputed with the current method by letting the time march to 6 seconds. The resulting temperature contours, temperature profiles and vorticity field was then compared with that of Keyes [11]. The solutions indicated that the resulting temperature field and flow field (with strong recirculations) compared very well with that of Keyes. The temperature profiles at 1.2 cm and 2.4 cm above the fuel exit have the same magnitude and location as Keyes predicted. The temperature at the center line of our results was about 100 degrees higher than that determined by Keyes.

II) Results for the 1 g case

Simulation of the experiments of Smyth, et al. [6] is started with the injection of both fuel and air into an initially quiescent domain. A flame front is assumed to form immediately at the reaction zone. The heated gas expands rapidly into the cold region as shown in Figure 1. As the flow continues to develop, the flame front moves further downstream. Due to the high temperature near the jet centerline, the fluid in the center region accelerates ahead of the rest of the jet. This fluid motion sets up a "mushroom" shape of the expanding gas as indicated in Figure 2. A strong vortex ring develops under the "mushroom" flame front as shown in Figure 3. As the flow evolves, the flame front eventually exits the computational domain. After the diffusion flame becomes fully developed into a quasi-steady state, it exhibits an average flame height of about 55.1 mm based on temperature profiles as shown in Figure 4. Figure 5 shows the experimentally observed OH laser-induced fluorescence and soot scattering images taken the study by Smyth, et al. [6]. Our numerical simulation yields a shorter flame compared to the visible flame height of 79 mm determined by the OH and soot images. Figure 6 shows the predicted maximum temperature location as a function of time for a total of five seconds. From this figure, we can see that during the first 0.3 seconds, the flame height oscillates with a magnitude of about 2.5 cm. This is due to the flow field adjusting to the massive changes in density and velocity. As the flow continues to develop, within the next 0.7 seconds, the diffusion flame develops a flickering behavior. After 1 second, the flickering behavior becomes repeatable. All the unsteady data (i.e., flickering frequency, emission index of NO_X and CO and their power spectra) are then obtained after this time. The power spectrum of this data (Figure 7) indicates that the flickering frequency is 15.7 Hz. The actual experimental frequency is 12 Hz [6]. For comparison, we note that a correlation developed in References 12, 13, and 14 indicates that the flickering frequency for a wide range of experiments is approximately given by $f \approx 1.5/D^{0.5}$, where D is fuel tube diameter in meters. The frequency obtained from this correlation is 14.3 Hz. This comparison demonstrates that our solution methodology is adequate for predicting the flickering frequency.

The emission indexes of NO_X and CO as a function of time for this flame at the exit plane are also calculated. The emission index of NO_X is defined as:

$$EI_{NO_X} = \frac{1}{Y_{fuel}} \frac{1}{\dot{M}_{fuel}} \left[\frac{MW_{NO_2}}{MW_{NO}} \dot{M}_{NO} + \dot{M}_{NO_2} \right]$$

where $\dot{M}$ is the mass flow rate, MW is the molecular weight, and Y is the mass fraction.

The emission index of CO is defined as:

$$EI_{CO} = \frac{1}{Y_{fuel}} \frac{1}{\dot{M}_{fuel}} \left[\dot{M}_{CO} \right]$$

As shown in Figure 8, the emission index of NO_X (EI_{NOX}) starts to grow after an elapsed time of 0.35 seconds. This is because the flame takes that long to propagate to the exit plane. The value of EI_{NOX} exhibits a high peak and then drops back to 0.8 g/Kg. This is due to the formation of an initial flame front with a much larger diameter than the fully developed flame diameter, resulting in a higher emission index than that for the fully developed flame. The value of EI_{NOX} continues to exhibit chaotic fluctuations up to a time of 1.6 seconds, when the fluctuations become repeatable. A power spectrum is then calculated from this data. The mean EI_{NOX} is 1.60 g/Kg with a standard deviation of 0.114 $(g/Kg)^2$. A similar analysis for the emission index of CO (EI_{CO}) (Figure 9) is also performed. The mean EI_{CO} is determined to be 79.0g/Kg with a standard deviation of 75.4 $(g/Kg)^2$.

Closer inspection of the instantaneous emission indexes for NO_X and CO indicated that the oscillations are also in phase. This is because the emission indexes are determined at the exit plane. As the fluid containing the burned gases exits the domain, the amount of NO_X and CO are determined simultaneously across that plane. Hence it is no surprise that the maximum and the minimum EI for NO_X and CO occur at the same instant. Further study of the entire instantaneous flame structure indicated that locally, those regions which have maximum concentration of NO_X have minimum CO concentration.

III) Results for the 0.5 g case

A second case with 0.5 g was simulated under the same conditions as in the 1 g case. The maximum temperature location along the center line as a function of time is shown in Figure 10. Reduction of the gravitational acceleration means that the buoyancy force is less then that of the 1 g case. The average flame height is now about 5.21 cm. The magnitude of the fluctuation is about 0.2 cm, which is also smaller than that of the 1 g case. The power spectrum of the instantaneous maximum temperature location along the center line (Figure 11) indicates that the flickering frequency is 8.3 Hz.

The emission index for NO_X is shown in Figure 12. One can see that the fluctuation is more complicated than that for the 1 g case. The power spectrum (Figure 13) of the emission index shows that the fluctuation consists of 2 frequencies: 8.3 Hz and 10.4 Hz. The mean EI_{NOX} for this case is 1.73 g/Kg with a standard deviation of 0.119 $(g/Kg)^2$. Similarly, the emission index for the CO (Figure 14) also contains these two frequencies. The mean EI_{CO} is 73.0 g/Kg with a standard deviation of 204 $(g/Kg)^2$.

IV) Results for the 2.0 g case

A third case with a body force twice that of the earth's gravitational force was included in the study. All the initial and boundary conditions are the same as in the 1 g case. With a stronger buoyancy force, the flame height is slightly higher than that of the 1 g case. The mean flame height of the 2 g case is at 5.91 cm with a fluctuation of 1 cm as shown in Figure 15. The flickering frequency is also higher than that for the 1 g case. The power spectrum (Figure 16) of the instantaneous maximum temperature along the center line location indicates that the flickering frequency is at 23.2 Hz. The power spectrum also picks up a second harmonic at 46.5 Hz. as shown in Figure 16. The emission index of NO_X is shown in Figure 17. The mean EI_{NOX} is 1.33 g/Kg with a very large fluctuation of 0.8 g/Kg. The standard deviation of the EI_{NOX} is 0.0899 $(g/Kg)^2$. The emission index of CO is also calculated under this condition. As shown in Figure 18, the mean value of EI_{CO} is 86.5 g/Kg with a fluctuation of 20 g/Kg. The standard deviation is 219 $(g/Kg)^2$.

V) Summary of the three cases in this study

The flickering frequency, mean maximum temperature location along the center line, and mean emission index of NO_X and CO with their standard deviations under various gravitational forces are summarized and listed in table 1.

Table 1
Summary of all time-averaged statistics.

G-Force	f (Hz)	$\overline{T_{max\,loc}}$ (cm)	$\sigma^2_{T_{max\,loc}}$ (cm^2)	$\overline{EI_{NOx}}$ (g/Kg)	σ^2_{NOx} $(g/Kg)^2$	$\overline{EI_{CO}}$ (g/Kg)	σ^2_{CO} $(g/Kg)^2$
0.5 g	8.27	5.21	6.83e-2	1.73	0.119	73.1	204.
1.0 g	15.7	5.51	1.87e-1	1.60	0.114	79.0	75.4
2.0 g	23.2	5.91	3.53e-1	1.33	8.99e-2	86.5	219.

The results indicate that as the gravitational force increases, the mean flame height increases by 5.8 percent from 0.5 g to 1 g and by 7.3 percent from 1 g to 2 g. However, the variance of the flame height increases dramatically by a factor of 2.7 from 0.5 g to 1 g and by a factor of 1.9 from 1 g to 2 g. This means that as the gravitational force increases, the fluctuation of the flame height increases. This can also be seen in Figures 6, 10, and 15. The results also indicate that as the gravitational force increases, the mean emission index for the NO_X decreases by 7.5 percent from 0.5 g to 1 g and by 16.9 percent from 1 g to 2 g while the mean emission index of CO increases by 8 percent from 0.5 g to 1 g and by 9.5 percent from 1 g to 2 g.

7. Approximate Analysis of the Flickering Instability

We now turn to a discussion of the origin of the oscillation of the flame. This question has been studied by a number of researchers (see References 12, 1, and 15 and the works

cited therein). Buckmaster and Peters [1] work with a similarity solution to a system of boundary-layer equations which describe the flow associated with a flame sheet. Mahalingam, et al. [15] obtain solutions for parallel flow which includes heat release due to chemical reactions. Their treatment includes premixed and nonpremixed flames, and allows for three-dimensional perturbations. In both of these works, a system of equations for the first-order perturbation of the basic viscous flow is obtained by an inviscid linearization of the equations.

The basic mechanism for the oscillation of flames as expounded in References 1 and 15 is the Kelvin-Helmholtz instability. This also appears to be true in the present work. It is clear that the conditions for such an instability exist, as there exists a jet of fast-moving fluid (the reacting gases and the reaction products) moving through the slower coflowing air. The vorticity in our calculations (see, e.g., Figure 19) exhibits the expected vortex rollup near the flame, and a more complex evolution downstream.

In this paper, we do not provide an analysis as broad as those given in References 1 and 15. Our consideration is limited to the particular laminar diffusion flame discussed here. In order to apply the theory of the Kelvin-Helmholtz type of instability to this flame, we need to determine appropriate velocity and density profiles. Within the constraints imposed by linear stability analysis, this is somewhat subjective. We adopt the usual approach of assuming an unperturbed flow that is approximately uniform in the axial (vertical) direction. This is not a particularly good assumption on the scale of the axial variation in the perturbed flow of interest, so we must make a choice. Figures 4, 19 and 20 show that most of the action occurs in the range 5 cm $\leq z \leq$ 10 cm. We therefore make the somewhat arbitrary choice of z = 7.5 cm as the point at which to obtain the profiles that we use for the unperturbed flow. Figure 21 shows the axial velocity and the density as a function of radial position (denoted x) at that location at a typical time in the oscillating flow with a gravitational acceleration of 1 g. The dashed lines in the figure show the piecewise linear profiles that are used in the stability analysis. (Piecewise linearity allows us to obtain a solution in closed form.) The values of density are held constant at ρ_1=0.24 g/cm^3 and ρ_2=1.17 g/cm^3. The coflow velocity at this location is maintained at w_{02} = 5.0 cm/s, but the central core velocity w_{01} varies according to the value of the gravitational acceleration. This variation will be discussed below. For the 1 g case, we set w_{01} = 255 cm/s.

We now make the approximation that the unperturbed flow is uniform in the axial direction, and look for axisymmetric modes of the form $h(r)\exp[i(kz-\omega t)]$, where h stands for any of the first-order flow variables. Since we seek only order-of-magnitude approximations and scaling laws, we assume slab geometry instead of the more appropriate (axisymmetric) cylindrical coordinates. (So r is replaced by the rectangular coordinate x.) Following the usual procedures (see, e.g., References 1, 15, and 16; in particular, Reference 16 contains material relevant to closed-form solutions), we obtain the following dis-

persion relation connecting the frequency and wave number:

$$[(\nu-\eta)(\tanh\eta\alpha+1)-\gamma][(\nu-\eta\beta)(\sigma+1)-\gamma]$$
$$-[(\nu-\eta)(\tanh\eta\alpha-1)-\gamma][(\nu-\eta\beta)(\sigma-1)-\gamma]e^{-2\eta\delta}=0 \qquad (8)$$

The dimensionless quantities appearing here are defined as follows: frequency $\nu=b\omega/w_{01}$, wave number $\eta=kb$, core radius $\alpha=a/b$, width of transition region $\delta=(b-a)/b$, coflow velocity $\beta=w_{02}/w_{01}$, velocity gradient in the transition region $\gamma=(\beta-1)/\delta$, and density ratio $\sigma=\rho_2/\rho_1$.

This differs from the analysis in Reference 1 in that approximate unperturbed velocity and density profiles are used instead of those obtained from a solution for the viscous flow solution to a model problem, and use is not made of boundary-layer approximations. It differs from that in Reference 15 in that slab geometry is used instead of cylindrical coordinates, and again, approximate unperturbed profiles are used.

As noted in References 1 and 15, the approach to be taken here is to look for convective waves which propagate upwards and are amplified in the upward direction. To this end, the frequency takes on real values and we seek solutions of the dispersion relation for which the imaginary part of the wave numbers is negative. Figure 22 is a plot of the spatial growth rate Im(η) versus the actual frequency f in Hz for our 1 g calculation. (It was obtained by solving the dispersion relation via Newton's method.) The low frequency (long-wavelength) modes are always unstable, although the spatial growth rate goes to zero as frequency goes to zero. There is a frequency limit above which the modes are stable (Im(η)=0). This is due to the nonzero thickness of the shear layer (see Figure 21) corresponding to finite vorticity (rather than the infinite vorticity of a vortex sheet) [16]. Hence, there is a maximum spatial growth rate, and the frequency to which this corresponds is to be taken as the frequency of oscillation of the flickering flame [1,15]. For our 1 g case, this frequency is 6.75 Hz, slightly less than half the actual value obtained from the full simulation.

It is of interest to consider the variation of the flicker frequency with the magnitude of the gravitational acceleration. In the approach to the problem that we have taken, g does not enter into the equations for the perturbed quantities. Rather, it plays a role only in accelerating the hot gases upwards, and thereby increasing the velocity w_{01} used in the stability analysis. A crude one-dimensional approach to calculating the velocity of the unperturbed flow yields

$$w_{01}=\sqrt{w_j^2+2\left(\frac{\rho_2}{\rho_1}-1\right)gz}$$

where w_j is the velocity at the jet orifice (z=0). Assuming z=7.5 cm as discussed above,

values of g equal to half and twice the normal acceleration of gravity at the earth's surface were used to obtain appropriate velocities w_{01}. The resulting flicker frequencies are plotted in Figure 23. It is seen that the calculated frequency is very nearly proportional to $g^{0.5}$. This is predictable from the fact that $\beta=w_{02}/w_{01}$ and w_j/w_{01} are both small; in the limit that these two quantities go to zero it is easily seen that Eq. (8) need only be solved once for given values of δ and σ. Then f scales as w_{01}/b, and w_{01} scales as $g^{0.5}$.

It is seen that the agreement of the linear analysis with the two-dimensional simulation is not very precise. However, it should be recalled that the analysis suffers from several defects: (1) The use of cylindrical coordinates instead of slab geometry would probably improve the agreement with experiment. (2) The assumption of axial invariance of the unperturbed configuration is not well-satisfied. (3) The analysis involves the linearization of a process that becomes nonlinear very rapidly. As expected, a nonlinear two-dimensional calculation is necessary to obtain a really good approximation to the experimental results.

Conclusion

The first five seconds of the formation of a methane-air diffusion flame has been simulated by using the low Mach number form of the Navier-Stokes equation. The chemistry part of the calculations is modeled by the flamelet method. This avoids solving the energy and species equations for which one needs to resolve chemical time scales that are much smaller than the characteristic fluid time scale. The use of a flamelet library enables the calculations to carried out very efficiently. This is because the fluid mechanics is only affected by the existence of a flame through the change in density where its value is supplied by the flamelet library. Since there is no source/sink term in the mixture fraction equation, the only constraint is that of the convective time scale. The quasi-steady state flame height and the natural flickering frequency of the diffusion flame under various magnitudes of gravitational forces have been predicted.

The instantaneous and time average of the emission indexes EI_{NOX} and EI_{CO} are also determined in this study. For the 0.5 g case, the results indicate that the instantaneous EI_{NOX} and EI_{CO} are composed of 2 main frequencies: 8.3 and 10.4 Hz. By increasing the gravitational force by a factor of 4 (from 0.5 g to 2 g), the frequency increases by 181 percent. The flame height under this condition only increases by 13.4 percent but the variance increases by 416 percent. With the increase in buoyancy force that leads to more intense flame stretching, a reduction of NO_X emission by 23.1 percent with an increase of CO emission by 18.3 percent was found. For all cases in this study, the instantaneous EI_{NOX} and EI_{CO} are in phase.

An analysis of the instability that gives rise to the flicker of laminar diffusion flames such as the one studied here has been presented. It is capable of providing a rough estimate of the frequency of the flicker, and of the variation of the frequency with the gravitational

force that helps to drive the instability. This analysis is necessarily crude; for quantitative calculations of the flickering behavior, the fully nonlinear simulation is required.

Future work

These results indicate the flickering frequency is a function of the magnitude the of gravitational force. Although the mean flame height increases slightly, the magnitude of the oscillation in flame height increases by a factor of 4 within the range of this study. A reduction of NO_X emission with an increase in CO emission was also observed. This may lead to a possible control of NO_X and CO emission by manually modulating the flickering frequency. Having confidence in this code, we can study the effects on emission index by manually pulsing the fuel inlet to vary the flickering frequency to investigate the changes in NO_X and CO emissions.

References

[1] Buckmaster, J., and Peters, N., "The Infinite Candle and its Stability—A Paradigm for Flickering Diffusion Flames," Twenty-First Symposium (International) on Combustion, p. 1829, The Combustion Institute, 1986.

[2] Yam, C., "A study of a Turbulent Diffusion Boundary Layer Flame," Master's Thesis. U.C. Davis, 1986.

[3] Peters, N., "Laminar Diffusion Flamelet Models In Non-Premixed Turbulent Combustion," Prog. Energy Combustion. Sci. **10**, pp. 319-339, 1984.

[4] Katta, V. R., Goss, L. P. and Roquemore, W. M., "Numerical Investigation of Transitional H_2/N_2 Jet Diffusion Flames," AIAA J., **32**, pp. 84-94, 1994.

[5] Kaplan, C. R., Baek, S. W., Oran, E. S. and Ellzey, J. L., "Dynamics of a Strongly Radiating Unsteady Ethylene Jet," Comb. & Flame, **96**, pp. 1-21, 1994.

[6] Smyth, K. C., Harrington, J. E., Johnson, E. L. and William, M. P., "Greatly Enhanced Soot Scattering in Flickering CH_4/Air Diffusion Flames," Comb. & Flame, **95**, pp. 229-239, 1993.

[7] Zel'dovich, Y. B. and Frank-Kamenetskii, D. A., "The Theory of Thermal Propagation of Flames," Zhur. Fiz. Khim. **12**, 100, 1938.

[8] Sharif, M. A. R. and Busnaina, A. M., "Assessment of Finite Difference Approximations for the Advection Term in the Simulation of Practical Flow Problems," J. Comp. Phys. **74**, pp. 143-176.

[9] Kim, J. and Moin, P., "Application of a Fractional-Step Method to Incompressible Navier-Stokes Equations," J. Computational Physics **59**, pp. 308-323 (1985).

[10] Chorin, A. J., "Numerical solution of the Navier-Stokes equations," Math. Computation **22**, pp. 745-762, 1968.

[11] Keyes, D., Philbin, D., and Smooke. M., "Modification and Improvement of Software for Modeling Multidimensional Reacting Fuel Flows," Wright Research Development Center, Aero Propulsion and Power Laboratory. Report Number WRDC-TR-89-2056

[12] Hamins, A., Yang, J. C., and Kashiwagi, T., "An Experimental Investigation of the Pulsation Frequency of Flames," Twenty-Fourth Symposium (International) on Combustion, The Combustion Institute, Pittsburgh, 1992, pp. 1695-1702.

[13] Zukoski, E. E., Cetegen, B. M., and Kubota, T., "Visible Structure of Buoyant Diffusion Flames," Twentieth Symposium (International) on Combustion, The Combustion Institute, Pittsburgh, 1984, pp. 361-366.

[14] Cetegen, B. M., and Ahmed, T. A., "Experiments on the Periodic Instability of Buoyant Plumes and Pool Fires," Comb. & Flame, **93**, 157-184 (1993).

[15] Mahalingam, S., Cantwell, B. J., and Ferziger, J. H., "Stability of low-speed reacting flows," Phys. Fluids A **3**, 1533 (1991).

[16] Drazin, P. G., and Reid, W. H., "Hydrodynamic Stability," Cambridge University Press, 1981.

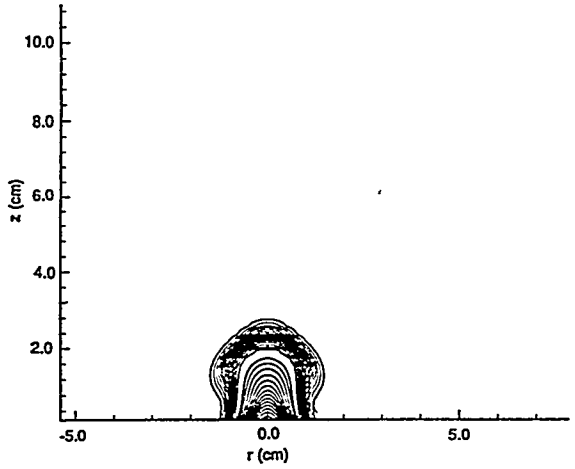

Figure 1. Temperature contours at 7.5×10^{-2} seconds.

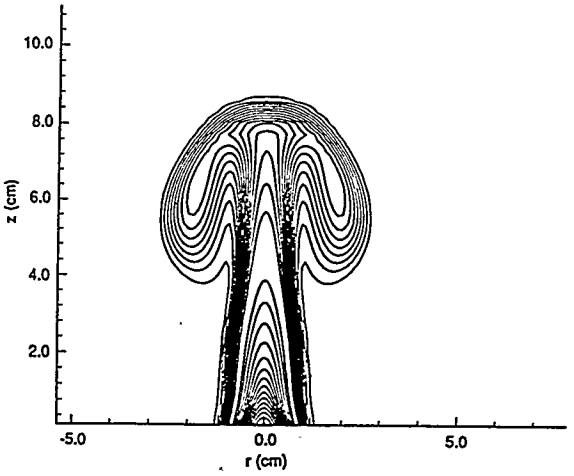

Figure 2. Temperature contours at 0.18 seconds.

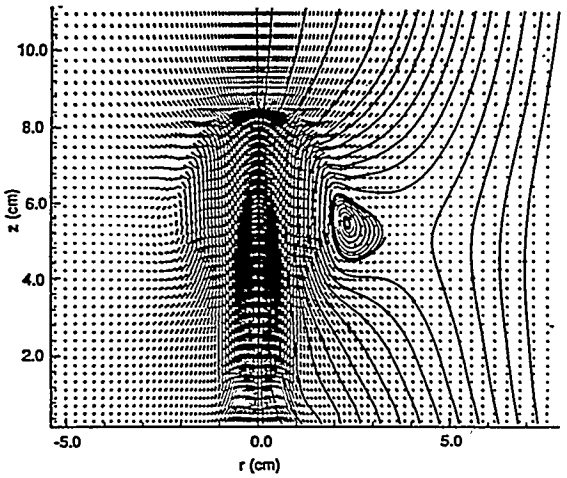

Figure 3. Velocity vectors and stream lines at 0.18 seconds.

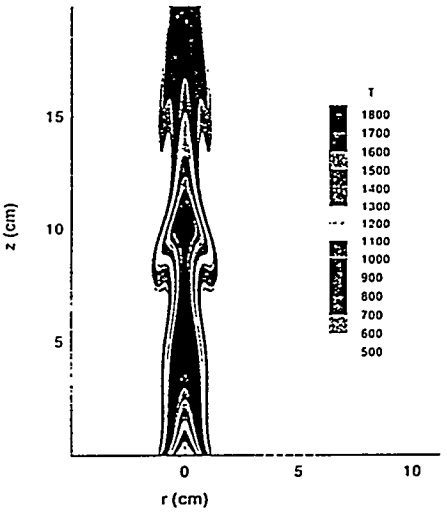

Figure 4. Temperature contours at "steady state".

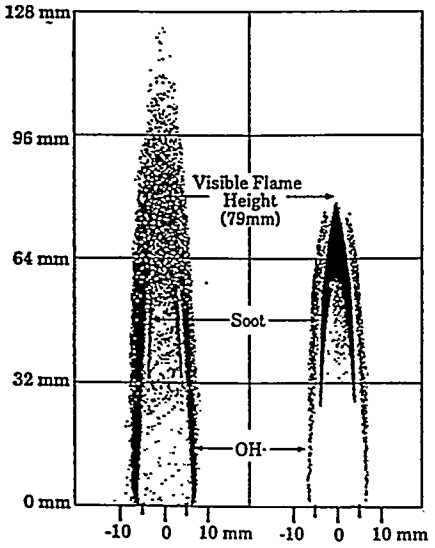

Figure 5. Image of steady state laminar flame at 1 g.

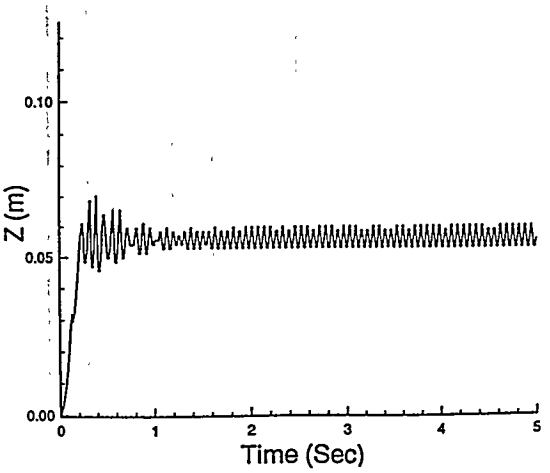

Figure 6. Maximum temperature location at the center line as a function of time at 1 g.

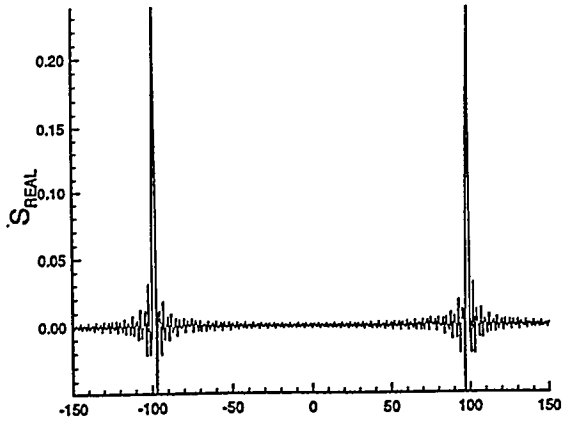

Figure 7. Power spectrum for the flickering frequency at 1 g.

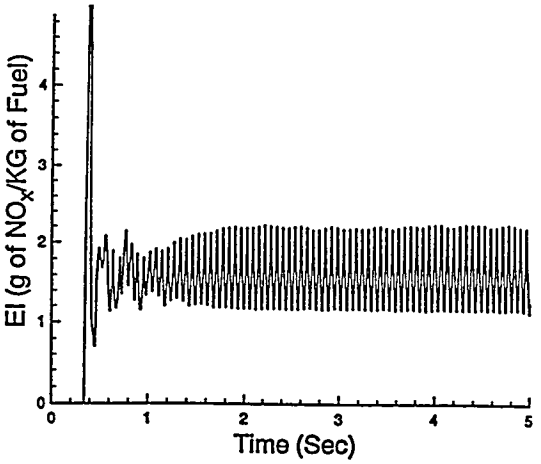

Figure 8. Emission index for NO_X at 1 g.

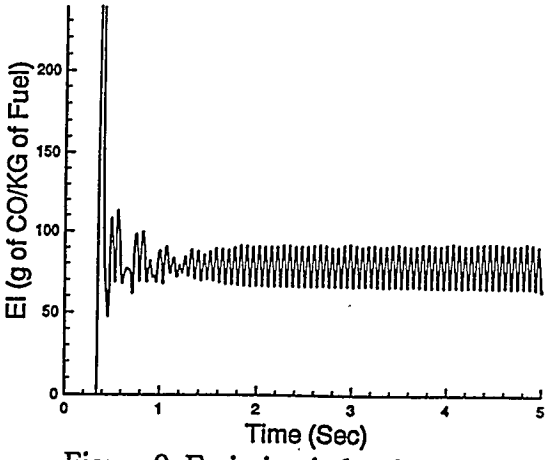

Figure 9. Emission index for CO at 1 g.

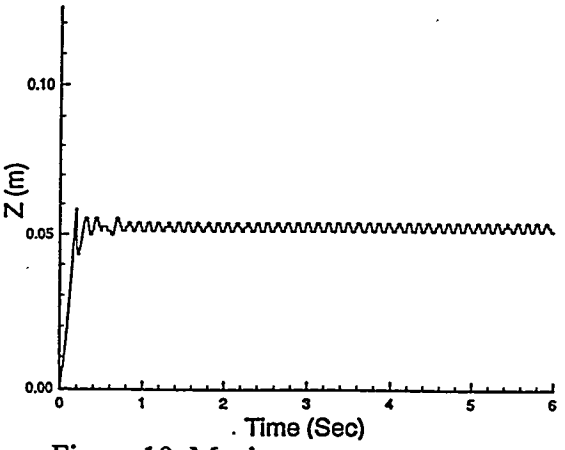

Figure 10. Maximum temperature location at the center line as a function of time at 0.5 g.

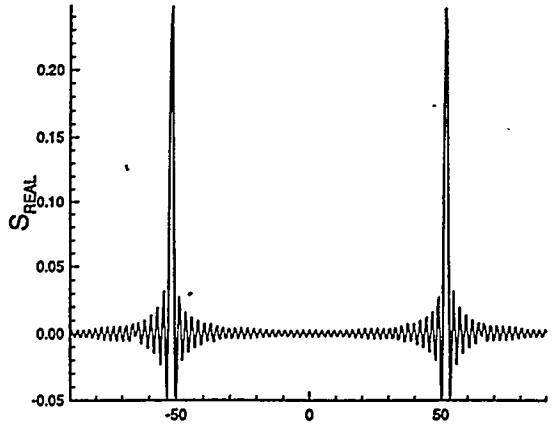

Figure 11. Power spectrum for the flickering frequency at 0.5 g.

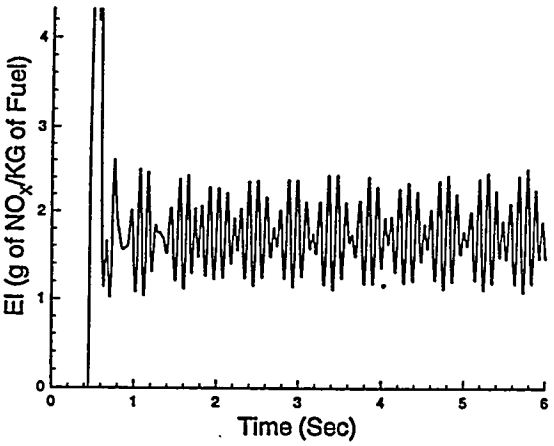

Figure 12. Emission index for NO_X at 0.5 g.

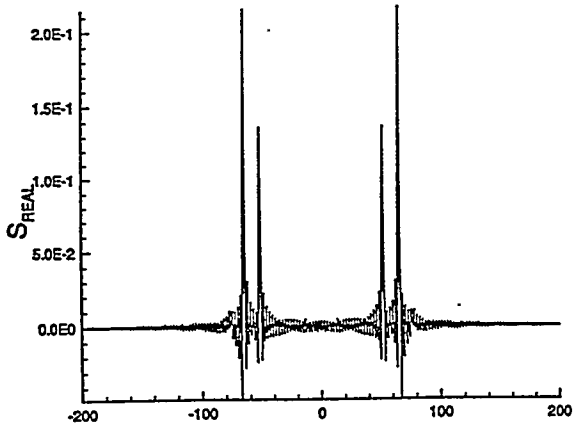

Figure 13. Power spectrum for the emission index for NO_X at 0.5 g.

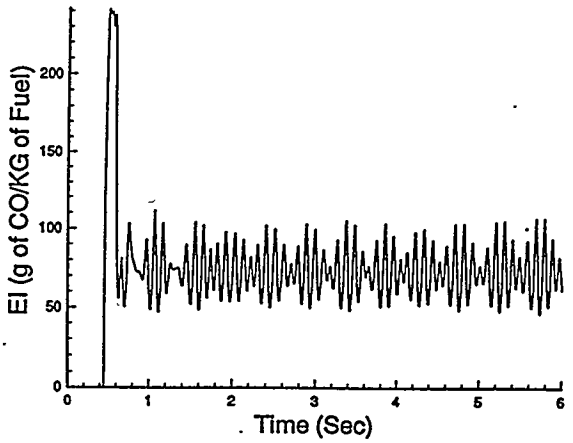

Figure 14. Emission index for CO at 0.5 g.

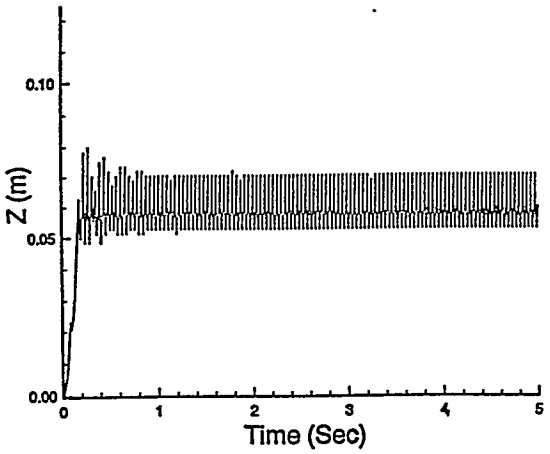

Figure 15. Maximum temperature location at the center line as a function of time at 2 g.

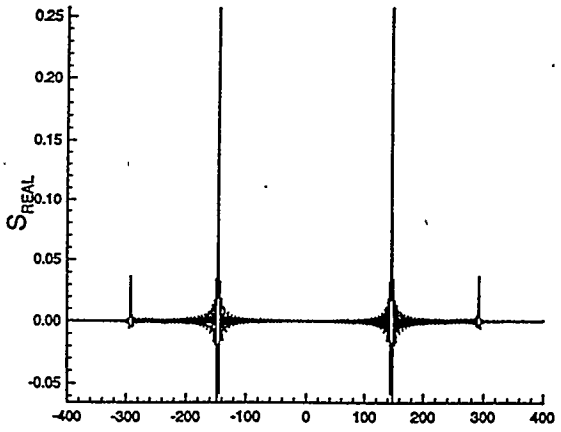

Figure 16. Power spectrum for the flickering frequency at 2 g.

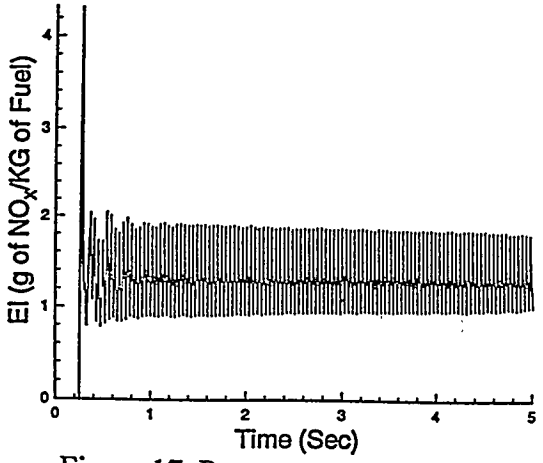

Figure 17. Power spectrum for the emission index for NO_X at 2 g.

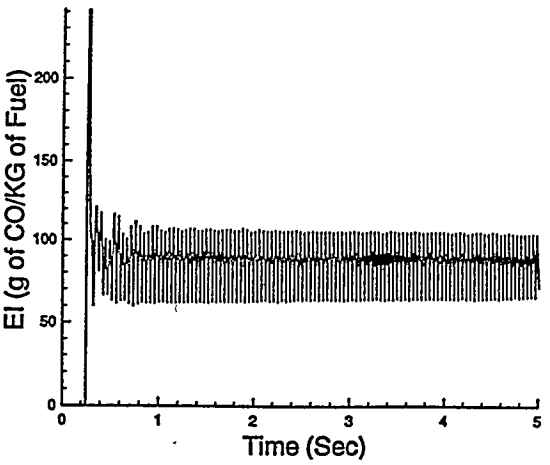

Figure 18. Emission index for CO at 2 g.

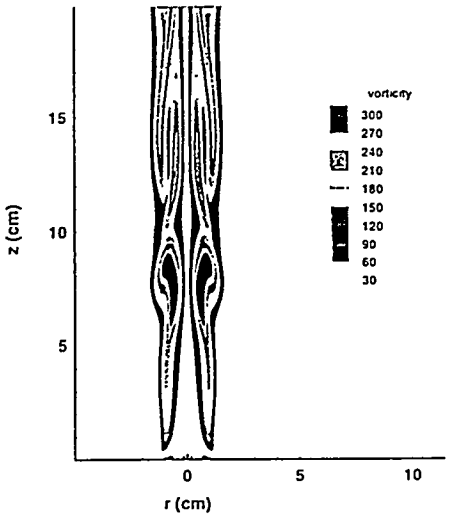

Figure 19. Contour plot of vorticity at a typical time in the oscillation cycle.

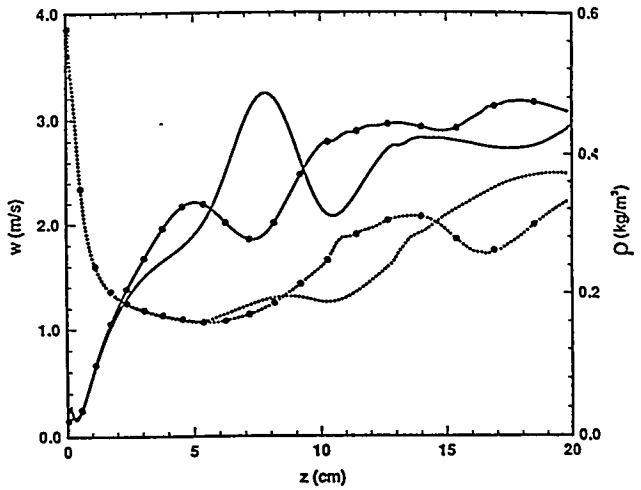

Figure 20. Velocity (solid lines) and density (dotted lines) versus axial coordinate z at two different times in an oscillation cycle. The plots with closed circles lag the others by approximately 180 degrees in phase angle.

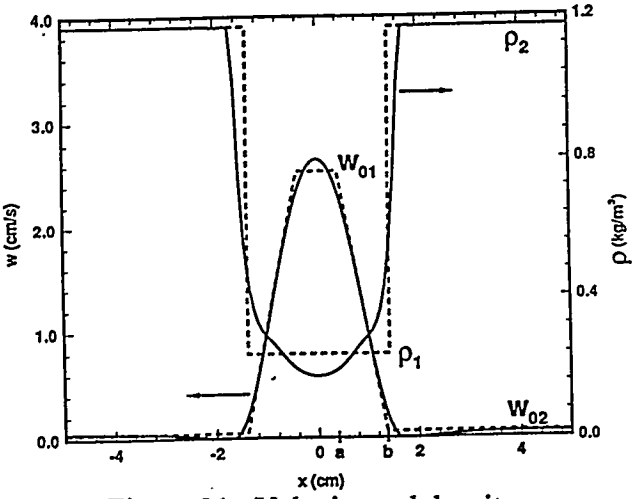

Figure 21. Velocity and density versus transverse coordinate x. Dashed lines show the piecewise linear profiles used in the analysis. These profiles are defined by the coordinates a and b, the velocities $w02$ and $w01$, and the densities ρ_2 and ρ_1.

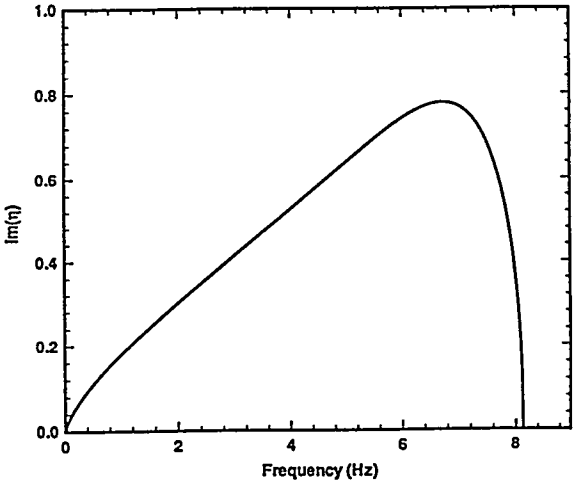

Figure 22. Spatial growth rate Im(η) versus frequency in Hz for the 1 g case.

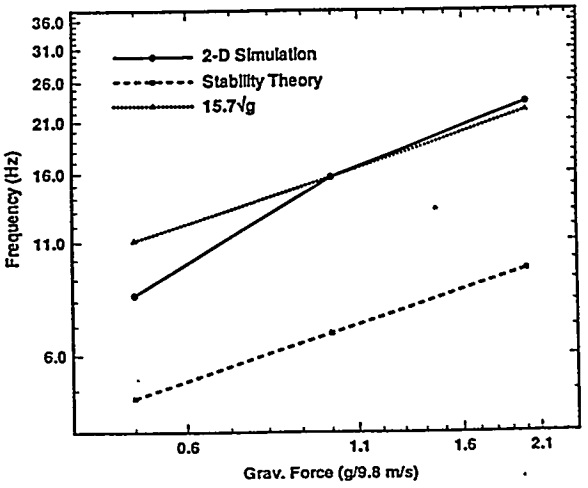

Figure 23. Flicker frequency as determined by the numerical simulation and by the stability analysis. The line proportional to $\sqrt{g}$ is given for comparison.